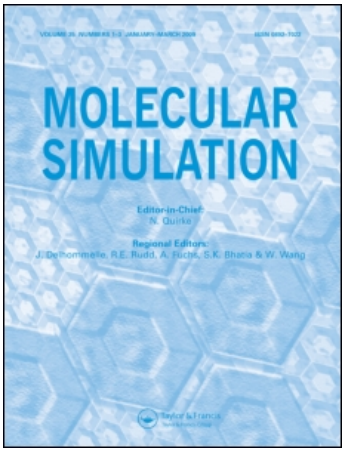

Molecular Simulation
Publication details, including instructions for authors and subscription information:
http://www.informaworld.com/smpp/title~content=t713644482

Atomistic behavior analysis of Cu nanowire under uniaxial tension with maximum local stress method

Y. C. Lin[a]; D. J. Pen[a]
[a] Department of Mechanical Engineering, National Taiwan University of Science and Technology, Taiwan, R.O.C

To cite this Article Lin, Y. C. and Pen, D. J.(2007) 'Atomistic behavior analysis of Cu nanowire under uniaxial tension with maximum local stress method', Molecular Simulation, 33: 12, 979 — 988
To link to this Article: DOI: 10.1080/08927020701502040
URL: http://dx.doi.org/10.1080/08927020701502040

Molecular Simulation, Vol. 33, No. 12, October 2007, 979–988

Taylor & Francis
Taylor & Francis Group

Atomistic behavior analysis of Cu nanowire under uniaxial tension with maximum local stress method

Y. C. LIN and D. J. PEN

Department of Mechanical Engineering, National Taiwan University of Science and Technology, 106 Taiwan, R.O.C

(Received March 2007; in final form June 2007)

This study analyzes the atomistic behaviors of a Cu nanowire (NW) during uniaxial tensile deformation by molecular dynamics simulation. In this work, the maximum local stress calculated method (MLS) is proposed to validly elucidate the plastic behaviors of the Cu NW. Analysis results demonstrate that the pre-tension stress is caused by the intense surface tension, which is an important factor for dislocation emission from surface. The motion of Shockley partials that interact to produce a stair-rod dislocation is determined. Following the dislocation mechanism, deformation twinning is the primary mechanism that dominates the plastic deformation at such a high strain rate. Immediately before fracture, the stress increases markedly since the primary failure mode is atomic bond breakage.

Keywords: Atomistic simulation; Nanowire; Plastic deformation; Dislocation nucleation

PACS: 31.15.Qg

1. Introduction

Surface-to-volume ratio (STVR) is increasing markedly when the scale of the components decreases to the nano scale. High STVR results in a large difference in the mechanical properties between nano scale and large scale component, strengthening the surface effects. Therefore, understanding the mechanical properties of metal NWs is the key to designing and fabricating nano- and micro-components.

Technology for manufacturing has been developed to produce metal nanofilms and NWs. The (100) Au nanofilms undergo a crystal orientation from (100) into (111) if the thickness of the nanofilm is smaller than 2 nm [1] and the cross-section of the thinnest NW is only four atomic rows [2]. However, performing a mechanical test on metallic NWs is difficult. Molecular dynamics (MD) provides a powerful method for analyzing the behaviors in a nano scale system. Hence, the vast theoretical analyses [3–20] have been performed investigating the unique deformation behaviors of metallic NWs. For example, at a higher strain rate ($7 \times 10^{10} s^{-1}$), the NWs can change from crystalline phase into an amorphous phase under simple tensile deformation [3]. Other researchers [4–13] investigated applied stress state (tension vs. compression), lattice orientation, size and strain rate effect in metallic NWs. In particular, certain metal NWs can be driven to undergo phase transformation by surface stress [14] and the phase transformation can exhibit both shape memory and pseudoelastic behavior [15–19]. However, previous research mostly focused the plastic deformation modes within initial yield period. Little attention [20] has been focuses on the plastic deformation mode transformations and the variation of flow stress of metallic NWs under uniaxial tension until broken.

The strength of nanowires (NW) was predicted mostly using the virial stress [21], which is determined by the average of all atomic stresses in the NW. Since elastic deformation occurs uniformly and simultaneously, this approach can properly express the elastic properties in elastic regime. However, plastic deformation does not occur uniformly and simultaneously. The stress should not be the same every where during plastic deformation. The stress of plastic deformation region is easily under-estimated, which arises from the averaging effect using the virial stress. Hence, the maximum local stress method (MLS) has been proposed to evaluate the flow stress of the NW during tensile plastic deformation process.

This study aims to investigate the various deformation modes of a Cu NW at different tensile stages through MD simulations and examines the validity of the MLS approach.

Molecular Simulation
ISSN 0892-7022 print/ISSN 1029-0435 online © 2007 Taylor & Francis
http://www.tandf.co.uk/journals
DOI: 10.1080/08927020701502040

2. Methodology

This investigation studies the mechanical behavior of the Cu NW under uniaxial tension using an MD simulation, assuming a perfectly FCC crystalline structure, as displayed in figure 1. The dimensions of the specimen are $7a \times 7a \times 20a$, where "a" is the lattice constant. The surface atoms in both x-[100] and y-[010] directions are free. The tensile load is applied in the z-[001] direction. Both the top and the bottom of the specimen are boundary atoms, colored red in the figure, which are used to control the strain and strain rate in the tensile test. In this work, the embedded-atom-method (EAM) potential, proposed by Johnson [22], is employed to describe the atomic interactions. The EAM function of total energy is given by

$$U_{\text{tot}} = \sum_i F_i(\rho_i) + \frac{1}{2}\sum_i \sum_{j \neq i} \phi_{ij}(r_{ij}) \tag{1}$$

$$\rho_i = \sum_{j \neq i} f(r_{ij}) \tag{2}$$

where i and j are the indices of the atoms; r_{ij} is the distance between atom i and atom j; F is the embedded energy; ρ is the electron cloud density, and ϕ is the pair potential. The physical properties of the potential compared to experimental data are found in table 1. Although the stacking fault energy of the Johnson model is lowers than that of some models (Voter and Chen (VC) and Mishin *et al.* (MF) models), the difference is unobvious for copper [23]. However, the shear constant and the vacancy formation energy of the Johnson model are fitted the experiment exactly.

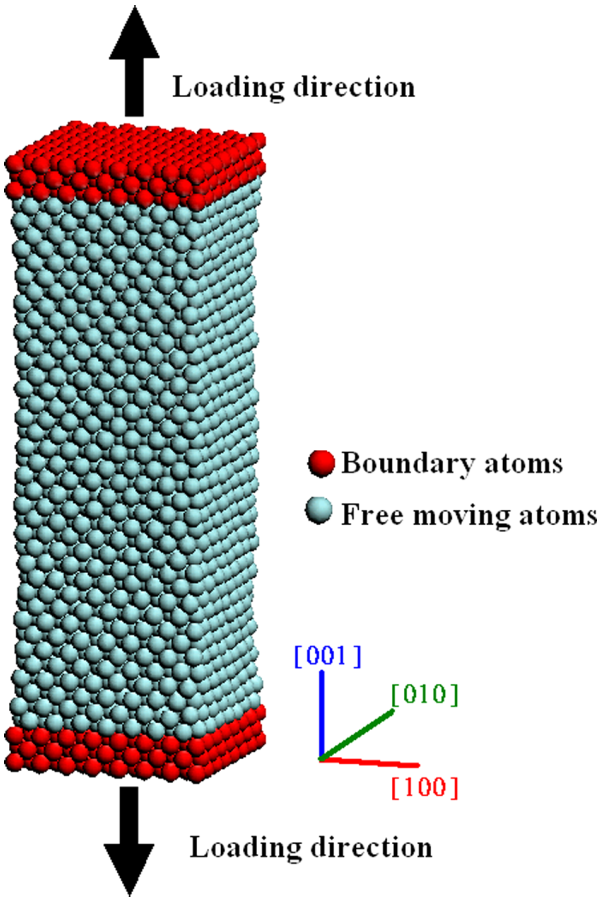

Figure 1. MD stimulation model for the Cu NW.

Table 1. The properties of the Johnson models[22,23].

Property	*Johnson model*	*Experiment*
Shear constant, G_e (10^{12}ergs/cm^3)	0.55	0.55
Unrelaxed vacancy-formation energy, E_{1v}^{VF} (eV)	1.305	1.306
Unstable stacking fault energy, γ_{us} (mJ/m^{-2})	158	
Intrinsic stacking fault energy, γ_{us} (mJ/m^{-2})	27	45
Surface energy, γ_{100}(mJ/m^{-2})	1200	
γ_{110}(mJ/m^{-2})	1300	1790[†]
γ_{111}(mJ/m^{-2})	990	

[†] The average surface energy.

The temperature condition of the system depends on the Maxwell distribution of total atomic kinetic energy in MD simulations. The desired temperature is 295 K by scaling the velocity of atoms. Computational parameters used in this work are listed in table 2.

The virial stress comprises a kinetic part and a potential part:

$$\bar{\sigma}_{mn}^{\text{virial}} = \frac{1}{V_{\text{total}}} \sum_{i=1} \left[m_i v_i^m v_i^n - \frac{1}{2} \sum_j \frac{\partial U(r_{ij})}{\partial r_{ij}} \frac{x_{ij}^m x_{ij}^n}{r_{ij}} \right] \tag{3}$$

where V_{total} is the total volume of the specimen; v_i^m is the velocity of atom i in the m direction, and x_{ij}^m is the component in the m direction of the distance between atoms i and j.

The atomic stress of atom i, as proposed by Basinski, Duesbery and Taylor (BDT) [24] and therefore called the BDT stress, is given by,

$$\sigma_{mn}^i = \frac{1}{V_i} \left[m_i v_i^m v_i^n - \frac{1}{2} \sum_j \frac{\partial U(r_{ij})}{\partial r_{ij}} \frac{x_{ij}^m x_{ij}^n}{r_{ij}} \right] \tag{4}$$

where V_i is the volume of atom i.

Table 2. Conditions of the MD simulation for uniaxial tension.

Potential function	*EAM*
NW dimensions	$7a \times 7a \times 20a$, where a is lattice constant (2.53 nn × 2.53 nm × 72.41 nm)
Boundary conditions	x-[100] and y-[010]:Free surfaces z-[001]: Boundary atoms on the top and bottom surfaces
Tensile direction	z-[001]
Strain rate	$7.07 \times 10^9\,\text{s}^{-1}$
NW temperature	295 K
The cutoff radius	1.9 r_o, $r_o = 0.256$ nm
Time step	1 fs

The mean stress of a specific region, developed by Miyazaki *et al.* [25], is expressed as follows;

$$\bar{\sigma}_{mn} = \frac{1}{N_S}\sum_i \sigma^i_{mn} \tag{5}$$

where N_s is the number of the atoms in the evaluated zone.

This study utilizes two methods for evaluating stress. The first calculates the virial stress that is through by the average of all atomic stresses in the NW, using the equation (3). The second unitizes MLS to evaluate the flow stress of the specimen during the tensile process. The following is the explanations of MLS. The tensile specimen is divided into ten zones along the tensile axis at every time step, as presented in figure 2. Initially, the local stresses of the each region are determined using equation (5). Then, the maximum stress among these local stresses is defined as the MLS of the tensile specimen. Theoretically, a region with a smaller cross-section area has a higher stress. Accordingly, MLS will be closer to the definition of the true stress than the virial stress during uniaxial tensile process.

The engineering strain rate is determined by calculating the variation with the initial length of the specimen in the [001] direction. Since the tensile axis represents the main strain direction, only the normal strain in the [001] direction at every time step needs to be calculated, according to,

$$\varepsilon_{[001]}(t) = \frac{L_{[001]}(t) - L_{[001]}(0)}{L_{[001]}(0)} \tag{6}$$

where $L_{[001]}(0)$ is the initial length of the NW, and $L_{[001]}(t)$ is the mean length in the [001] direction at every time step.

After the initial positions of the atoms are located, the specimen fixed by boundary atoms is relaxed to the equilibrium state at a particular constant temperature. The top and bottom boundary atoms are moved in opposite directions at equal speed, as displayed in figure 1. Furthermore, no scaling temperature is applied to the specimen during the uniaxial tensile process. Hence, the system follows an adiabatic process.

3. Results and discussion

3.1 Difference between virial stress and MLS

Figure 3 plots the stress–strain curves for the specimen under uniaxial tension by different approaches. The difference between the virial stress and MLS is unobvious in the elastic regime. However, the difference between the two methods is more obvious when the stress exceeded first peak. The virial stress declines gradually with the strain increasing and is even lower than the stress at beginning of extension. In contrast, MLS tends to increase with strain and rises dramatically before the specimen is broken. The local stress of the plastic deformation regions is continuously focused using MLS during tensile process. Therefore, the work hardening phenomenon is observed when stress is evaluated by MLS.

The result clearly shows that the virial stress cannot accurately describe the real plastic behaviors of the NW due to the averaging effect of overall atoms.

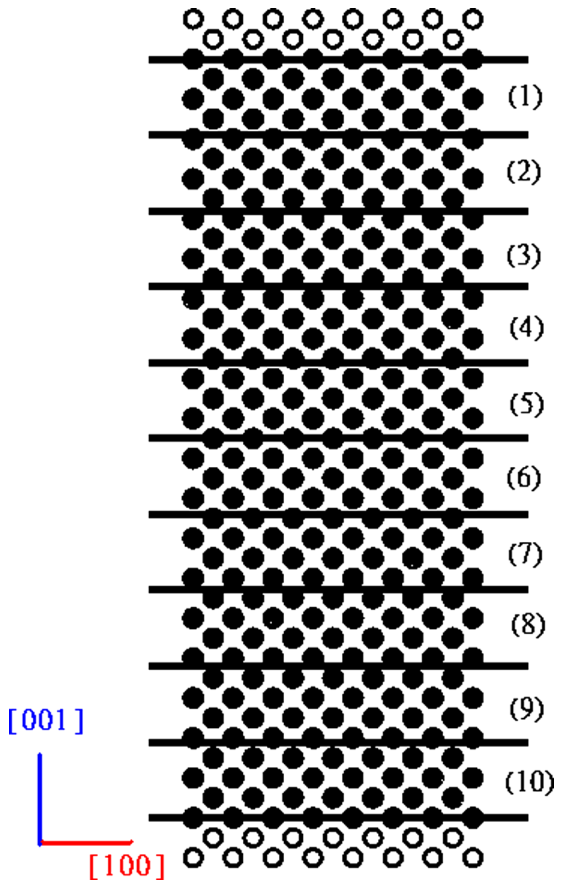

Figure 2. Schematic illustration for the maximum local stress method (MLS).

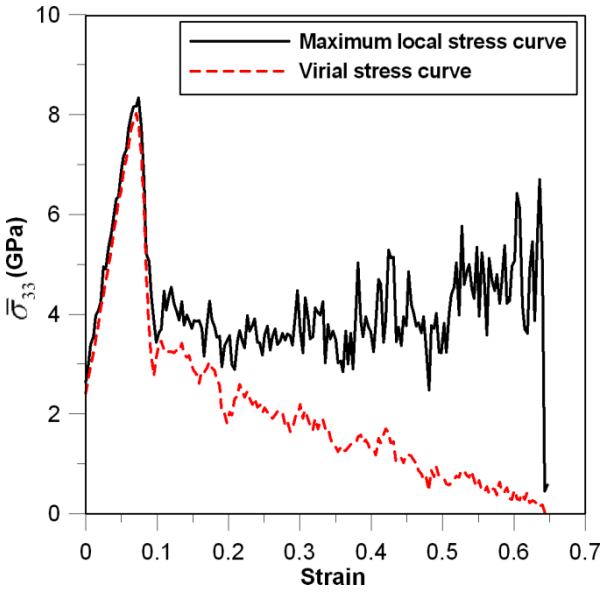

Figure 3. Stress–strain curves.

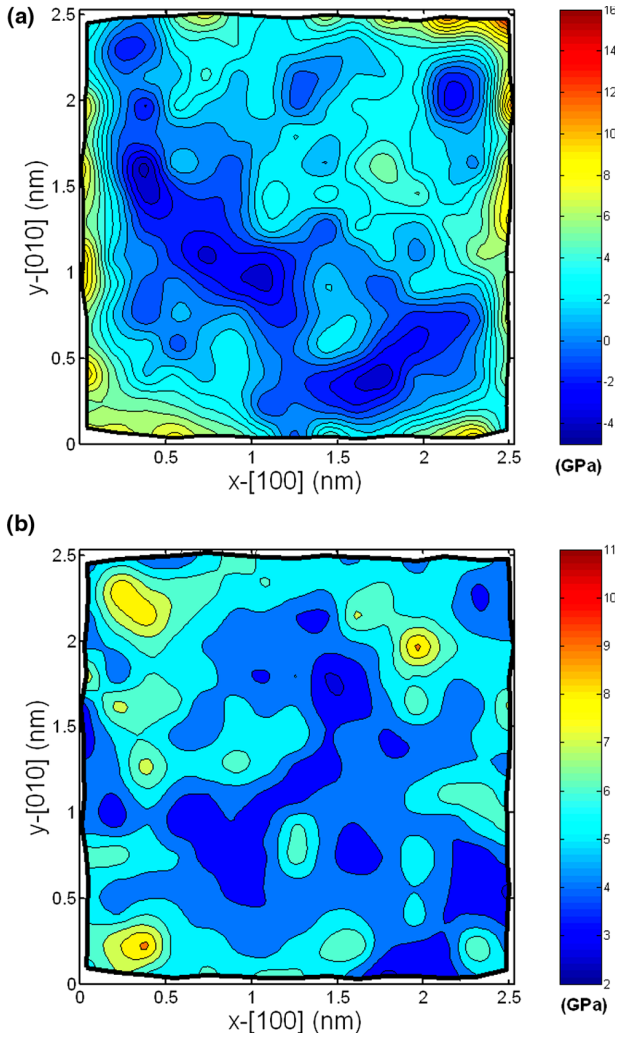

Figure 4. The contour of the atomic stress (a) normal stress σ_{zz} distribution and (b) the maximum shear stress τ_{max} in the middle cross plane of the NW after equilibrium.

However, MLS can reduce the averaging effect and yield the more accurate flow stress in the specimen. Therefore, the following deformation mechanisms are interpreted by MLS.

3.2 Pre-stress phenomenon

The tensile stress in the fixed specimen is 2.39 GPa immediately before the beginning of the uniaxial tensile process, as presented in figure 3. The existence of tensile stress at the beginning of extension is explained as follows. Surface layer atoms are attracted by atoms inside the specimen due to the bonding force. In contrast, no bonding force attracts the surface layer atoms in the direction from the surface to the outside. Hence, the asymmetric bonding force makes the lateral distance ([010], [100]) between atomic layers near the surface is shorter than those inside the specimen. This phenomenon is called layer relaxation [26] and similar phenomenon was found [8]. Moreover, figure 4(a) shows the contour of the atomic normal stress σ_{zz} distribution in the cross-section of the specimen before the tensile process. The layer relaxation effect causes the surface to contract and form a concave shape, making the distance between atoms in the z-direction near the surface is longer than inside. Therefore, the pre-strain effect increases the surface tension near the surface of the specimen. That is, the strong effects of surface stress are responsible for the pre-stress phenomenon, and cause the maximum shear stress of cross-section in the corners of the specimen, as shown in figure 4(b).

If the pre-tensile stress is relaxed to a zero stress state, surface stress can cause the ⟨100⟩/{100} orientation transform into the ⟨110⟩/{111} orientation herein. The phase transformation is both reversible and pseudoelastic, which has been studied in extensive literature [14–19]. Since the investigation mainly focus on the plastic deformation of the ⟨100⟩ NW, the relaxation of pre-tensile stress is unnecessary. A similar simulation method was employed when the cross-sectional area of a ⟨100⟩ gold NW is less than 2.45 × 2.45 nm [12].

3.3 Elastic deformation behavior

Before the stress arrives the first peak point, the stress increases approximately linearly with strain. Accordingly, the stress at the first peak point is defined as the yield stress of the tensile specimen. The yield stress is 8.34 GPa, accompanying a strain of 0.074. Before yielding, the linear part of the stress–strain curve is elastic deformation, and the slope of the curve is the elastic modulus, which is fitted to be around 82.8 GPa. This value slightly exceeds the bulk experimental result [27], which is approximately 67 GPa. However, the specimen herein is a perfect single crystal but this perfect state does not exist for traditional bulk materials. Hence, the slight discrepancy between the simulated and the experimental results of elastic modulus being 19.08 per cent is reasonable.

3.4 Dislocations and twinning mechanism operation during plastic deformation

Figure 5 plots the stress–strain curve during dislocation nucleation. At a strain of 0.064 (point A in figure 5), a leading partial dislocation with a Burgers vector $\vec{b}_1 = a/6[\bar{1}2\bar{1}]$ on the (111) slip plane is emitted from the surface, as shown in figure 6, indicated by arrow 1. Figure 7 displays the cutaway and vertical view of the active (111) slip plane in the specimen. The radius of the displayed atoms is halved to observe clearly the motion of the atoms on the (111) slip plane. The slipped atoms, the dark green atoms, below the arrow in figure 7(a), were originally located on the upright triangular gaps, which are constructed from the not slipped atoms, represented in turquoise in figure 7(a). Then, the slipped atoms move from the upright triangular gap to the inverted triangular gap on the (111) plane by the mechanism of partial dislocation slipping, as presented in figure 7(b). In the meantime, the specimen exhibits microstrain behavior before yielding.

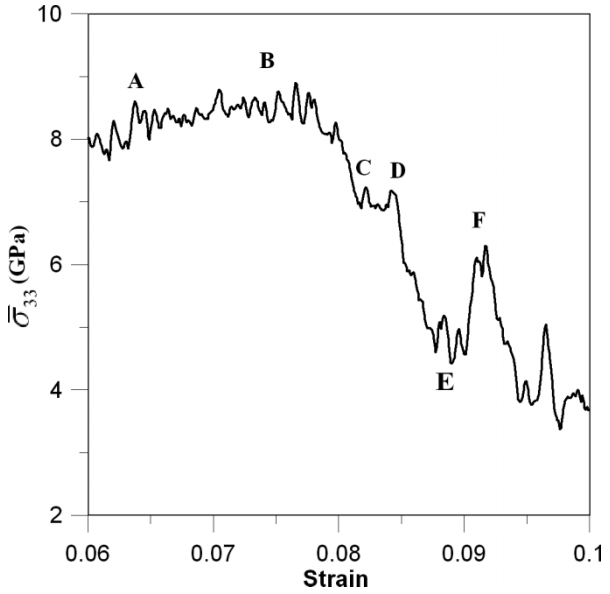

Figure 5. Stress(MLS)–strain curve in detail during dislocation nucleation.

Next, another leading partial with a Burgers vector $\vec{b}_4 = a/6[1\bar{2}\bar{1}]$ is emitted from surface when the strain is 0.068, indicated by arrow 2 in figure 6. The above $\vec{b}_1$ and $\vec{b}_4$ leading partials slipped on the (111) and (11$\bar{1}$)planes, respectively, and their subsequent slip is as shown in figure 8. The leading partials dislocations move to intersect with each other and form a Lomer–Cottrell lock (stair-rod dislocation), as presented in figure 8(b). The reaction can be explained in following way.

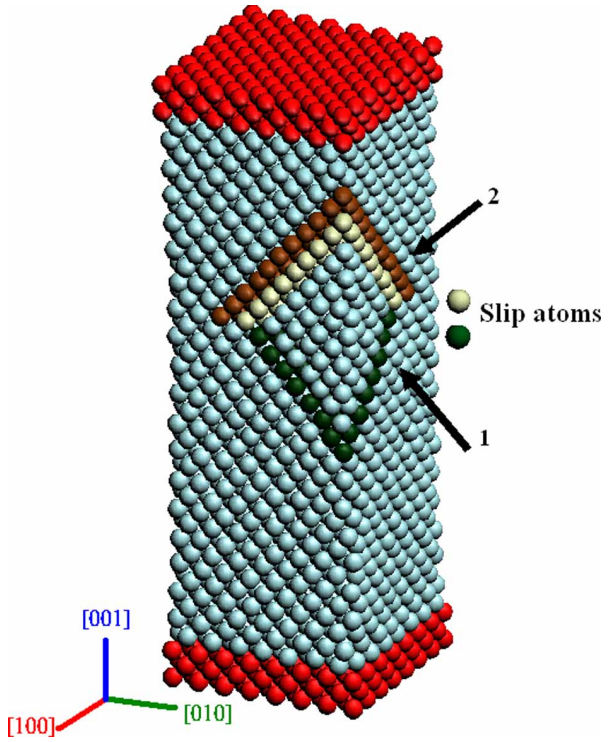

Figure 6. The positions of dislocation emissions from surface.

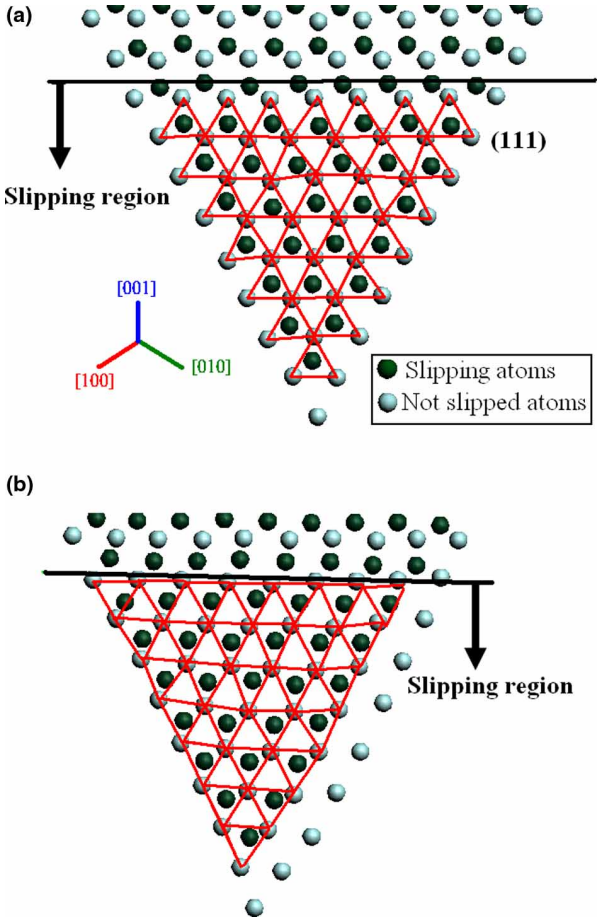

Figure 7. Motion of the first partial dislocation (a) strain = 0 and (b) strain = 0.08.

Figure 9(a) indicates that the two perfect dislocations, $\vec{b}_3 = a/2[01\bar{1}]$ and $\vec{b}_6 = a/2[0\bar{1}\bar{1}]$, originally glide on slip planes, and the two perfect dislocations can be dissociated to form a pair partials, respectively, as displayed in figure 9(b). The leading partials, $\vec{b}_1$ and $\vec{b}_4$, meet at the line of intersection of the two planes in the $[1\bar{1}0]$ direction, as shown in figure 9(c). The combination reaction is

$$\frac{a}{6}[\bar{1}2\bar{1}] + \frac{a}{6}[1\bar{2}\bar{1}] \rightarrow \frac{a}{3}[00\bar{1}] \tag{7}$$

The leading partials combine to form a stair-rod dislocation with a Burgers vector of $a/3[00\bar{1}]$ in order to reduce the strain energy. The plane which the stair-rod dislocation lies in can be determined as follows:

$$[1\bar{1}0] \times [00\bar{1}] = [110] \tag{8}$$

It cannot slip on the (110) plane because the plane is not a glide plane in an FCC crystal. Therefore, an obstacle to partial dislocations gliding in the (111) and (11$\bar{1}$) planes are formed, increasing flow stress beyond the point *A* in figure 5. Thereafter, the stress reaches its highest point associated with yielding (point *B* in figure 5). Next, the trailing partials, $\vec{b}_2$ and $\vec{b}_5$, glide on the region (stacking fault) of the slip planes that is not blocked by the stair-rod

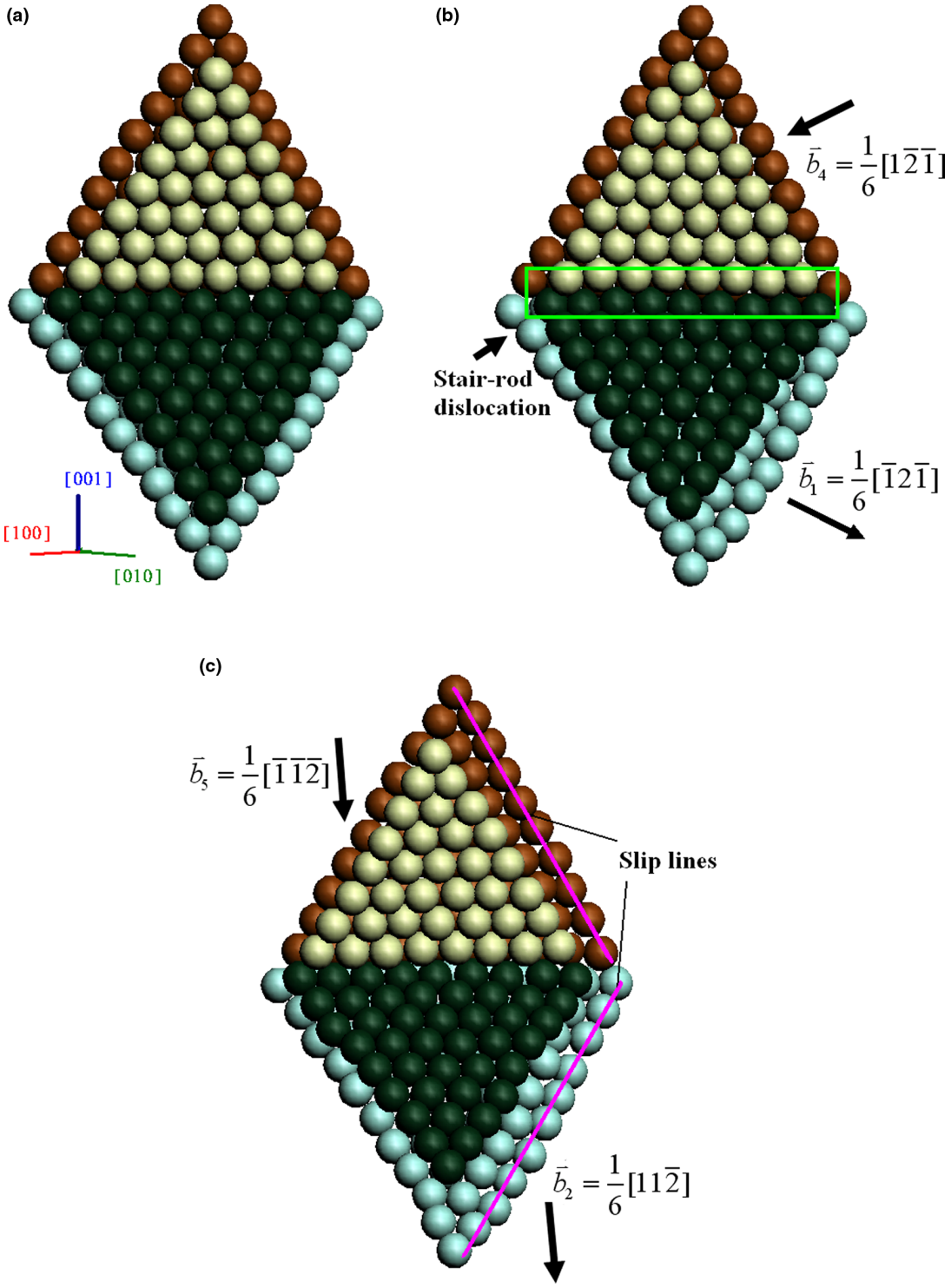

Figure 8. Dynamic evolution of the motion of dislocations, (a) strain = 0.6, (b) strain = 0.073 and (c) strain = 0.08.

dislocation. Hence, the stress for the following slip is reduced beyond the yield point. After the trailing partials have slipped on the (111) and (11$\bar{1}$)planes, the extra row steps, called slip lines, are clearly visible in the slipped region in figure 8(c).

When the stress approaches point *C* in figure 5, the trailing partials is close to the stair-rod dislocation. The resistance of the slipping partials is increased, causing slight strengthening, as shown in the region between points *C* and *D* in figure 5.When the strain reaches 0.083 (at point *D* in figure 5), the stair-rod dislocation changes into a micro-void-like feature, as presented in figure 10. Then, the stress clearly falls again. Moreover, the extra half planes of edge dislocations are also observed, indicated by arrows C_1 and C_2 respectively in figure 11(b). Simultaneously, another leading partial of the ($\bar{1}1\bar{1}$)[121]

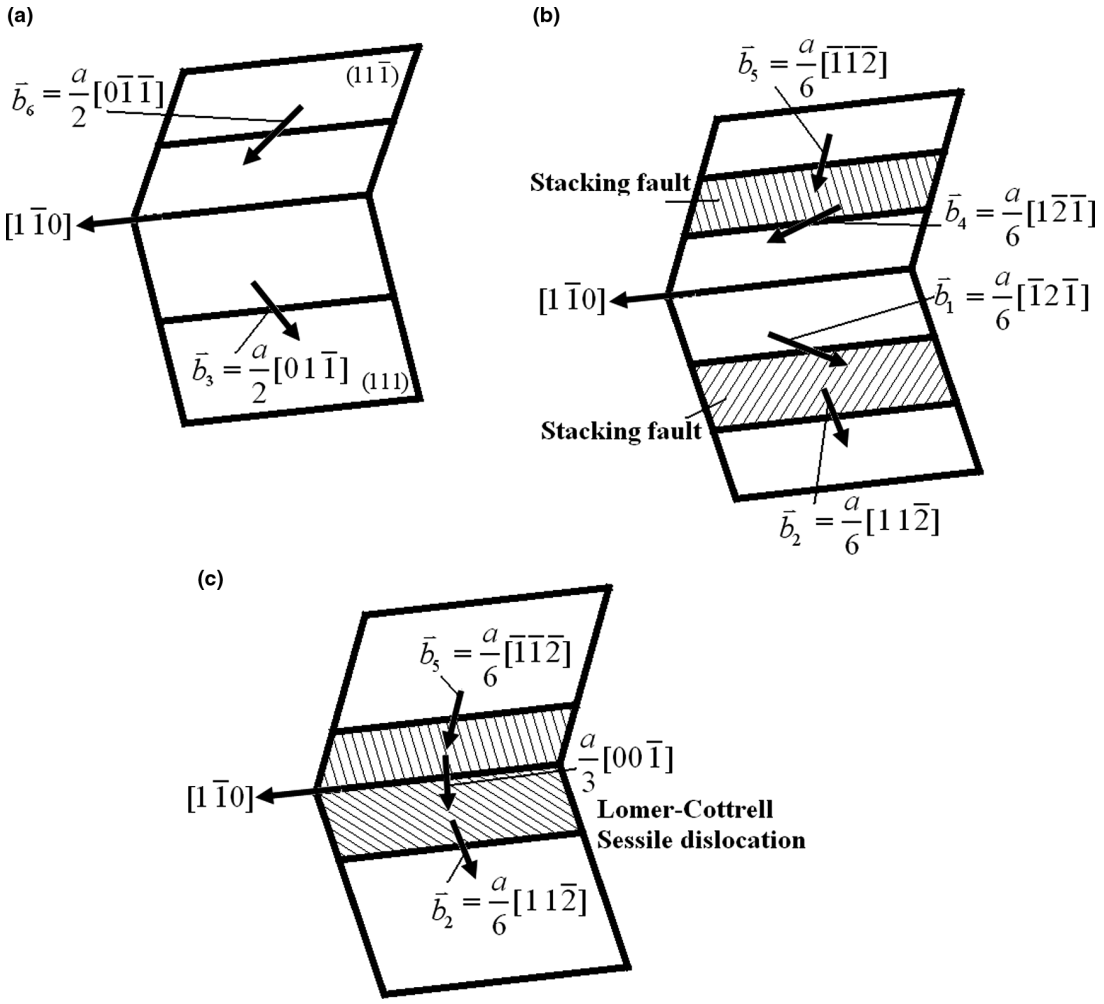

Figure 9. Schematic illustration of the formation of the Lomer–Cottrell sessile dislocation, (a) the original perfect dislocations, (b) the Shocky partial dislocations and (c) the formation of stair-rod dislocation.

type is emitted from the surface of the specimen, indicated by arrow D_1 in figure 11(b). The deformation twin, $(\bar{1}1\bar{1})[\bar{2}\bar{1}1]$ system, is also observed in the NW, as displayed in figure 11(c). Hence, the stress falls markedly until the twinning band was formed, as shown at point *E* in figure 5. However, the stress must be increased in order to drive the new deformation twinning, causing the stress to reach point *F* in figure 5. Upon a new twinning operation, the stress declines again. The rising and falling effect yields a serrate stress–strain curve, produced by deformation twinning. Extensive plastic deformation then begins.

In polycrystalline materials, the grain boundaries, associated with longitudinal incompatibility, cause stress concentration, so the most of the sources of dislocation emission are from the grain boundaries [28]. However, a single crystal NW has no grain boundaries, but strong surface effects that result from high STVR. Therefore, higher stress regions are always in surface layer, which is an important source of emitted dislocations. Under tension, before dislocation nucleation, the surface stress increases continually, along with the maximum shear

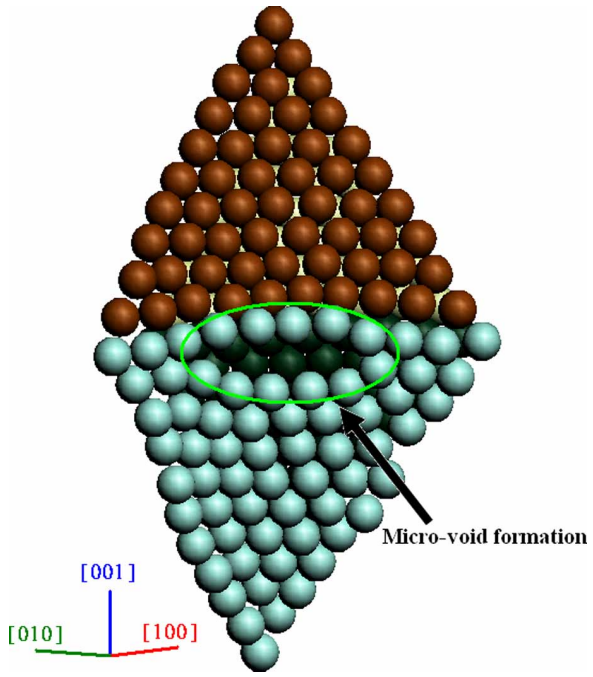

Figure 10. Formation of micro-void-like feature (strain = 0.083).

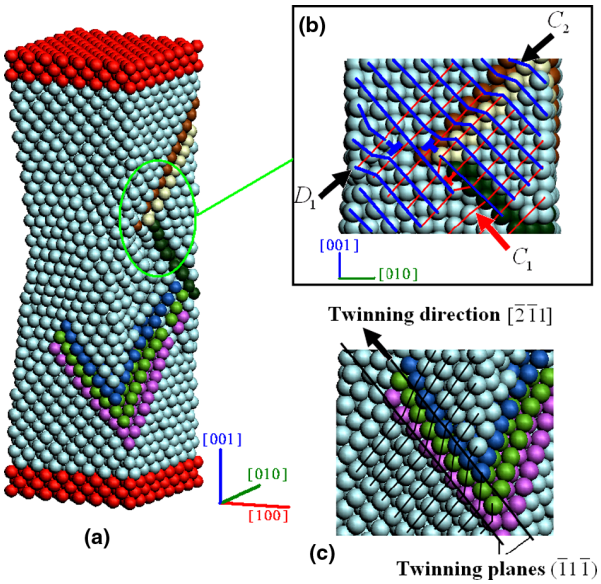

Figure 11. Features of the Cu nano wire at strain 0.084 (a) the entire NW, (b) side view and (c) the magnification of the local nano wire.

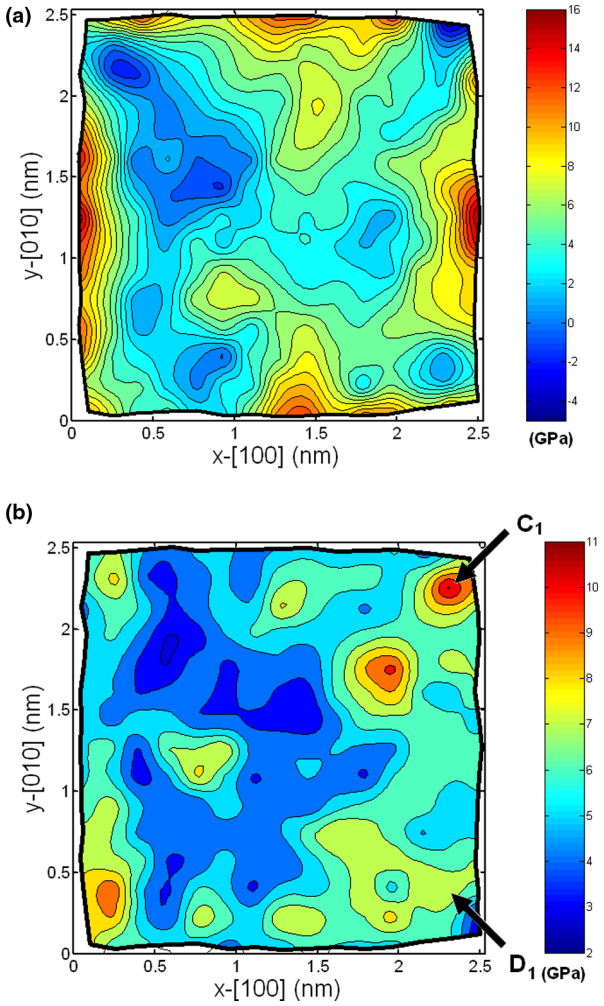

Figure 12. The contour of the atomic stress (a) normal stress σ_{33} distribution and (b) the maximum shear stress τ_{max}(strain = 0.05).

stress on the surface, as presented in figure 12. The regions of higher shear stress, indicated by C_1 and D_1 in figure 12(b), correspond to the surface regions indicated by C_1 and D_1 in figure 11(b). When the resolved shear stress reaches the critical shear stress, at those regions of high shear stress, partial dislocations are emitted from the surface, resulting in the microstrain behavior.

The active energy for dislocation operation is lower than that for twinning; therefore, dislocation slip is operated firstly. However, after initial yielding, twinning deformation contributes the most plastic deformation under high strain rate condition because the rate of plastic deformation by dislocation mechanism is lower than that by twining. Hence, twinning is following the dislocation slip herein.

3.5 *Necking and failure*

After the specimen experiences the dislocations gliding and twinning, the cross-sectional area in the middle of the NW was decreased slightly. That is, a little necking feature is produced, increasing the stress in the middle of the specimen, as displayed in figure 11(a). The high strain rate causes the twinning mechanism to mostly dominate the large plastic deformation with strains from 0.1 to 0.5. Therefore, the difference between the lattice orientation of the twinned and the untwinned regions is very clear, as displayed in figure 13. When the strain exceeds 0.5, more slips occur in the necked region by multiple slip systems. At that time, the area of the cross-section clearly contracts and is only several atoms in wide when the strain is 0.64, as shown in figure 14. Prior to fracture, the high normal stress σ_{zz} exists in the necking region and induces the atomic bond disconnecting and specimen breaking. Hence, the flow stress increases dramatically to 6.7 GPa and there is good evidence to show that MLS can validly character the variation of flow stress of NWs under tension.

The above observation is different from the previous research [4], indicated that at strain rate lower than $1.67 \times 10^8\,s^{-1}$, plastic deformation arises from nucleation and propagation of partial dislocations along the ⟨100⟩ NWs length. Since the strain rate ($7.07 \times 10^9\,s^{-1}$), in the study, is higher than the previous research, the dislocation slips and twins occurs sequentially during tensile process. Hence, at lower strain rate ($7.07 \times 10^7\,s^{-1}$), the added ⟨100⟩ NW is simulated to examine the validity of the simulation herein. Figure 15 shows that the NW reveals the sequentially propagation of partial dislocations pointed by a serious of arrows, which is consistent with the previous literature under low strain rate.

4. Conclusion

This investigation studies the atomistic behavior of the Cu NW with a rectangular cross-section under single tensile deformation, using EAM to perform a simulation.

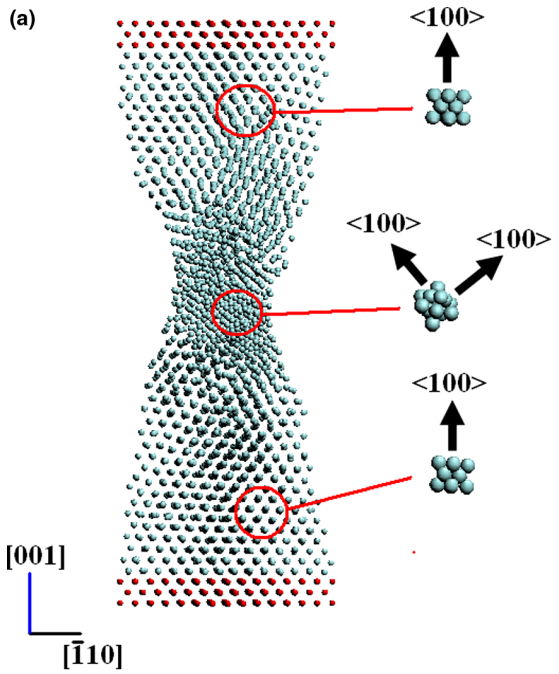

Figure 13. Snapshots of twinning in the Cu NW (a) strain = 0.3 and (b) strain = 0.5.

The mechanisms of deformation during the various stages—elastic deformation, dislocation nucleation, necking, and extensive plastic deformation—were examined. The following conclusions are drawn.

1. The new calculation method, MLS, is proposed to evaluate validly the variation in flow stress in the NW.
2. In the NW, the intense surface effect results in the pretension stress before extension. The surface stress causes dislocations to be emitted from the surface easily and is an important source of dislocation nucleation.
3. Under microstrain, even when global yielding has not yet occurred, partial dislocations were emitted from the surface. Additionally, the partial dislocations slip successively and meet to form the Lomer–Cottrell lock, resulting in a slight strengthening.
4. Following dislocation slipped, twinning becomes the primary plastic deformation mechanism at a high strain rate ($7.07 \times 10^9\,s^{-1}$). Just before fracture, atomic bond breakage is the major failure mode, increasing significantly the flow stress.

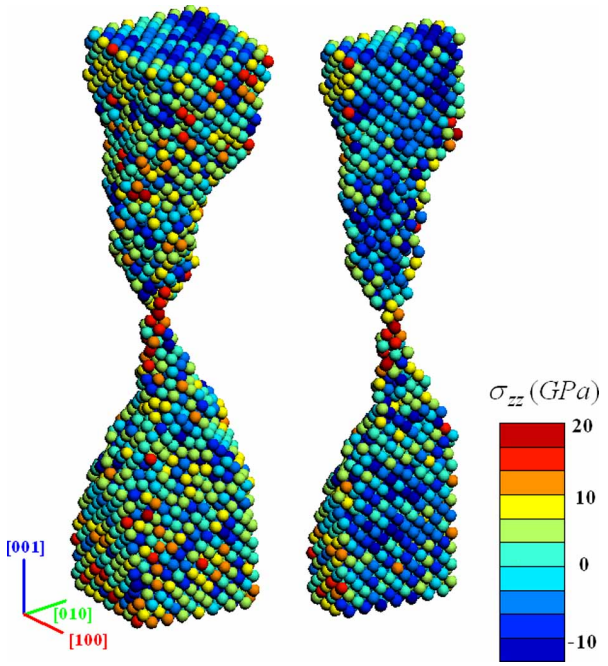

Figure 14. Normal stress σ_{33} distribution in the NW at a strain of 0.64.

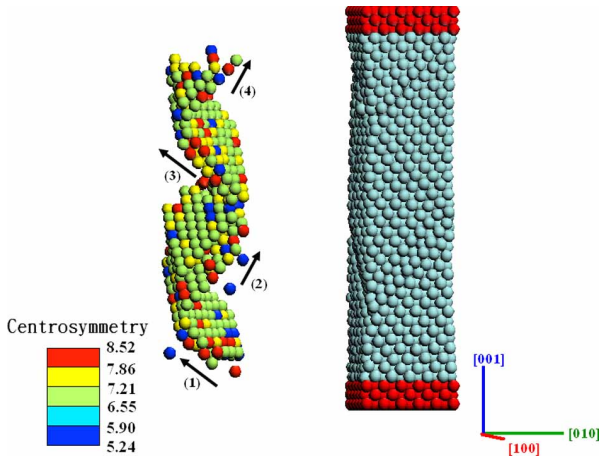

Figure 15. Right: snapshot of the Cu NW at strain of $\varepsilon = 0.053$. Left: Only atoms involved in defect and atoms colored by the centrosymmetry parameter (Kelchner *et al.* [29]).

References

[1] Y. Kondo, Q. Ru, K. Takayanagi. Thickness induced structural phase transition of gold nanofilm. *Phys. Rev. Lett.*, **82**, 751 (1999).

[2] Y. Kondo, K. Takayanagi. Gold nanobridge stabilized by surface structure. *Phys. Rev. Lett.*, **79**, 3455 (1997).

[3] H. Ikeda, Y. Qi, T. Cagin, K. Samwer, W.L. Johnson, W.A. Goddard III. Strain rate induced amorphization in metallic nanowires. *Phys. Rev. Lett.*, **82**, 2900 (1999).

[4] W. Liang, M. Zhou. Response of copper nanowires in dynamic tensile deformation. *J. Mech. Eng. Sci.*, **218**, 599 (2004).

[5] H.A. Wu. Molecular dynamics study on mechanics of metal nanowires. *Mech. Res. Commun.*, **33**, 9 (2006).

[6] H.A. Wu. Molecular dynamics of study the mechanics of metal nanowires at finite temperature. *Eur. J. Mech. A Solids*, **25**, 370 (2006).

[7] Z.C. Lin, J.C. Hung. A study on a rigid body boundary layer interface force model for stress calculation and stress–strain behaviour of nano scale uniaxial tension. *Nanotechnology*, **15**, 1509 (2004).

[8] S.J.A. Koh, H.P. Lee. Molecular dynamics simulation of size and strain rate dependent mechanical response of fcc metallic nanowires. *Nanotechnology*, **17**, 3451 (2006).

[9] H.S. Park, J.A. Zimmerman. Modeling inelasticity and failure in gold nanowires. *Phys. Rev. B*, **72**, 054106 (2005).

[10] H.S. Park, J.A. Zimmerman. Stable nanobridge formation in ⟨110⟩ gold nanowires under tensile deformation. *Scr. Mater.*, **54**, 1127 (2006).

[11] H.S. Park, K. Gall, J.A. Zimmerman. Deformation of FCC nanowires by twinning and slip. *J. Mech. Phys. Solids*, **54**, 1862 (2006).

[12] J. Diao, K. Gall, M.L. Dunn, J.A. Zimmerman. Atomistic simulations of the yielding of gold nanowires. *Acta Mater.*, **54**, 643 (2006).

[13] R.S. McEntire, Y.L. Shen. An atomistic analysis of incipient metal plasticity during tensile loading. *Mol. Simul.*, **32**, 857 (2006).

[14] J. Diao, K. Gall, M.L. Dunn. Surface-stress-induced phase transformation in metal nanowires. *Nat. Mater.*, **2**, 656 (2003).

[15] W. Liang, M. Zhou. Pseudoelasticity of single crystalline Cu nanowires through reversible lattice reorientations. *J. Eng. Mater. Technol.*, **127**, 423 (2005).

[16] W. Liang, M. Zhou, F. Ke. Shape memory effect in Cu nanowires. *Nano Lett.*, **5**, 2039 (2005).

[17] W. Liang, M. Zhou. Atomistic simulations reveal shape memory of fcc metal nanowires. *Phys. Rev B*, **73**, 115409 (2006).

[18] H.S. Park, K. Gall, J.A. Zimmerman. Shape memory and pseudoelasticity in metal nanowires. *Phys. Rev. Lett.*, **95**, 255504 (2005).

[19] H.S. Park, C. Ji. On the thermomechanical deformation of sliver shape memory nanowires. *Acta Mater.*, **54**, 2645 (2006).

[20] W.J. Kang, H.J. Hwang. Mechanical deformation study of copper nanowire using atomistic simulation. *Nanotechnology*, **12**, 295 (2001).

[21] R. Clausius. On a mechanical theory applicable to heat. *Phil. Mag.*, **40**, 122 (1870).

[22] R.A. Johnson. Analytic nearest-neighbor model for fcc metals. *Phys. Rev. B*, **37**, 3924 (1988).

[23] J.A. Zimmerman, H. Gao, F.F. Abraham. Generealized stacking fault energies for embedded atom FCC metals. *Model. Simul. Mater. Sci. Eng.*, **8**, 103 (2000).

[24] Z.S. Basinski, M.S. Duesbery, R. Taylor. Influence of shear stress on screw dislocations in a model sodium lattice. *Can. J. Phys.*, **49**, 2160 (1971).

[25] N. Miyazaki, S. Shiozaki. Calculation of mechanical properties of solids using molecular dynamics method. *JSME Int. J. A*, **39**, 606 (1996).

[26] K. Christmann. *Introduction to Surface Physical Chemistry*, Springr-Verlag, New York (1991).

[27] T.H. Courtney. *Mechanical Behavior of Materials*, 2nd ed., McGraw-Hill, Singapore (2000).

[28] M.A. Meyers, E. Ashworth. A model for the effect of grain size on the yield stress of metals. *Phil. Mag.*, **46**, 737 (1982).

[29] C.L. Kelchner, S.J. Plimpton, J.C. Hamilton. Dislocation nucleation and defect structure during surface indentation. *Phys. Rev. B*, **58**, 11085 (1998).